Weld Cracking in Duplex Stainless Steel (Report II)†

—Modelling of Cellular Dendritic Growth during Weld Solidification —

Fukuhisa MATSUDA*, Hiroji NAKAGAWA** and Jong-Bong LEE***

Abstract

A two dimensional solidification modelling of cellular dendritic growth was proposed in order to study the weld solidification phenomena of stainless steels in detail. The modelling was made based on the quenched solidification microstructures. Fraction solid vs. temperature and segregations of the solutes within the cellular dendrite were calculated by means of finite difference method.

Main conclusions obtained are as follows: (1) In this modelling, fraction solid increases very rapidly near liquidus temperature, and thus the temperature where the beginning of solid bridge is formed is very close to the liquidus temperature. (2) Therefore, the temperature zone where residual liquid is confined by the solid bridges is very long. (3) These behaviors mentioned in (1) and (2) fits well with the actual solidification microstructures. On the other hand, parabolic growth model where solid-liquid interface advances in proportion to square root of time does not fit with the actual microstructure. (4) Distributions of Ni and Cr in cellular dendrite calculated corresponded well to the EPMA analysis.

It was concluded that the two dimensional modelling is very useful to understand the weld solidification phenomena compared with conventional models.

KEY WORDS: (Computation) (Segregation) (Solidification) (Stainless Steels)

1. Introduction

The authors showed[1] that the weld metal of duplex stainless steel is more susceptible to solidification crack than those of type 304 and 430 stainless steel, although it is less susceptible than that of type 310S. In order to study the reason of this tendency, liquid-tin quenching was carried out for the purpose to freeze solidification microstructure[2–4] during welding. This intensive quenching revealed these interesting behaviors: (1) Solid bridge between secondary dendrite arms growing from the neighbouring primary dendrite arms was formed at a very high temperature near solidification front. (2) Due to the developing of the solid bridge, residual liquid droplets are confined to the intersectional site of the primary and the secondary dendrite arm boundary. (3) In the weld metal solidifying with primary ferrite, cellular dendritic microstructure becomes obscure rapidly with a decrease in temperature even in the solid-liquid coexistent region. Especially, the secondary dendrite arm boundary becomes obscure easily. These findings, with the aid of quantitative evaluation of microsegregation, should give very important clues to interpret the crack susceptibilities. Unfortunately, however, the quantitative evaluation of microsegregation is generally difficult in weld metal because of the size of resolution power of EDX or EPMA which is comparative to the secondary dendrite arm spacing in weld metal. This problem has stimulated the authors to analyze the behavior by making a modelling of cellular dendrites which matches with the findings metioned above.

Until now, many kinds of modellings of dendritic solidification have been proposed. In most of them, dendritic solidification has been approximated as unidirectional solidification which advances generally perpendicularly to the secondary dendrite arm or sometimes in parallel with the secondary dendrite arm. Among them. E. Scheil's equation[5] is the simplest one. As well known, however, this equation has a very severe limitation due to the neglect of the solute diffusion in solid. Therefore, H.D. Brody *et al.*[6] improved E. Scheil's equation, and T.W. Clyne *et al.*[7] improved H.D. Brody's equation. On the other hand. I. Ohnaka[8] derived another more precise equation using a profile method. Recently, S. Kobayashi[9] solved this problem rigorously by an analytical method.

In spite of these improvement, these analyses have a crucial disadvantage for the author's purpose, because any unidirectional model cannot deal with the formation of solid bridge and thus the resultant confinement of residual liquid to the intersectional site between primary and secondary dendrite arm boundary. Recently, two or three dimensional modelling of cellular dendrite was proposed by several researchers[8,10–12], although

† Received on May 8, 1989
* Professor
** Instructor
*** Graduate Student

Transactions of JWRI is published by Welding Research Institute of Osaka University, Ibaraki, Osaka 567, Japan

T. Matsumiya *et al.*'s and I. Ohnaka's modelling are not strict two dimensional ones. Among them, T. Matsumiya's model[10] took account of the formation of solid bridge due to contact of adjoining dendrites, but secondary dendrite arm is ignored because of an approximation of dendrite to hexagonal cell. D.G. McCartney *et al.*[11,12] made a three dimensional modelling to get stationary shape of dendrite without any secondary arm, and the formation of solid bridge was not taken account of. Therefore, all the modelling proposed untill now is not available for the purpose of this study.

In this paper, therefore, another type of two dimensional modelling of dendritic growth was proposed, by which the behaviors obtained by liquid-tin quenching mentioned above can be explained. The usefulness of the modelling was checked by EPMA analysis on microsegregation. The final aim of the model is to reveal the tendency of solidification crack susceptibility, and the results are discussed in the next paper[13].

2. Materials and Experimental Procedure

2. Material used

The chemical compositions of commercial stainless steels used, namely SUS329J2L, SUS310S and SUS430 are listed in **Table 1** with their thickness. The solidification crack susceptibility and the solidification sequence of these materials were already studied by the Trans-Varestraint test[1] and the liquid-tin quenching method[2-4], respectively.

2.2 Experimental procedure

Distributions of Ni and Cr concentrations in the cellular dendrite of quenched specimens[2-4] were analyzed by EMPA point analysis. The analyzing conditions used were accelerating voltage of 15kV and specimen current of 4nA and measuring time of 30sec. All of the data was corrected by the ZAF method.

3. Numerical Analysis

3.1 Two dimensional model of cellular dendrite

Growth model of the cellular dendrite was made based on the authors' own results[2-4] revealed by liquid-tin quenching. **Figure 1** explains the two dimensional model used. The solidification sequence based on the results of liquid-tin quenching is illustrated in **(a)**, although its right half is reduced considerably in the transverse direction for the purpose of simplification. Solid bridges between secondary dendrite arms growing from the neighbouring primary dendrite arms are formed at a very high temperature near solidification front[2-4]. Due to the developing of the solid bridge, residual liquid droplets are confined to the intersectional site of the primary and the secondary dendrite arm boundary. Rectangle OHPW in (a) is one volume element for numerical analysis. The lengths $\overline{OH}$ and $\overline{OW}$ correspond to one halves of primary and secondary dendrite arm spacing, respectively. In this model, as shown in **(b)**–①, solidification in OHPW starts from O, and the solid-liquid interface advances at a right angle to $\overline{WH}$. Solid bridges are formed at H and W at the stage shown in **(b)**–②. This means that the solid bridges in this model are formed at fraction solid of 50%. Then, the residual liquid is gradually confind to the region near P, where solidification finishes, as shown in **(b)**–③. Its details are shown in **(c)** with coordinates x and y. The solid-liquid interface has a terraced shape. In the model used, the number of division n_x in x direction is the same as the number n_y in y direction in this paper. In this paper, $n_x \times n_y$ is named the total number of division N_T.

3.2 Assumptions

Main assumptions adopted are as follows:

(1) Solute concentration in liquid is uniform. This might be roughly reasonable because of high diffusivity in liquid[14].

(2) Solute diffusion in solid has a temperature dependence, but has no concentration dependence.

(3) Local quilibrium always exists at the solid-liquid interface. In other words, solute is redistributed at the solid-liquid interface by equilibrium partition coefficient. Equilibrium partition coefficient is constant irrespective of temperature and concentration. Supercooling due to the curvature of solid-liquid interface and supercooling required for kinematics for advance of the solid-liquid

Table 1 Chemical compositions of materials used.

Material	Chemical composition (wt.%)								
	C	Si	Mn	P	S	Cr	Ni	Mo	N
SUS329J2L	0.017	0.57	1.57	0.028	0.001	22.13	5.49	2.92	0.14
SUS310S	0.070	0.61	1.67	0.022	0.001	24.78	19.14	0.06	0.03
SUS430	0.070	0.64	0.57	0.027	0.005	16.24	0.42	0.05	0.01

Thickness : 12mm

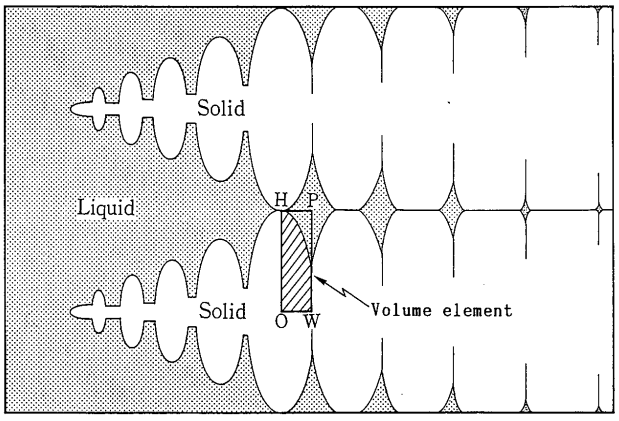

(a) Definition of volume element

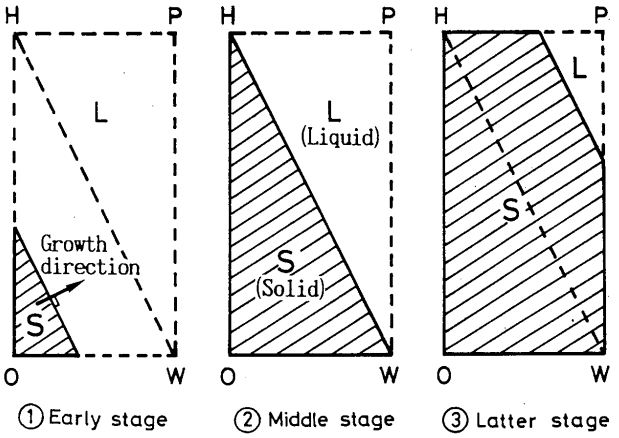

(b) Solidification process in volume element

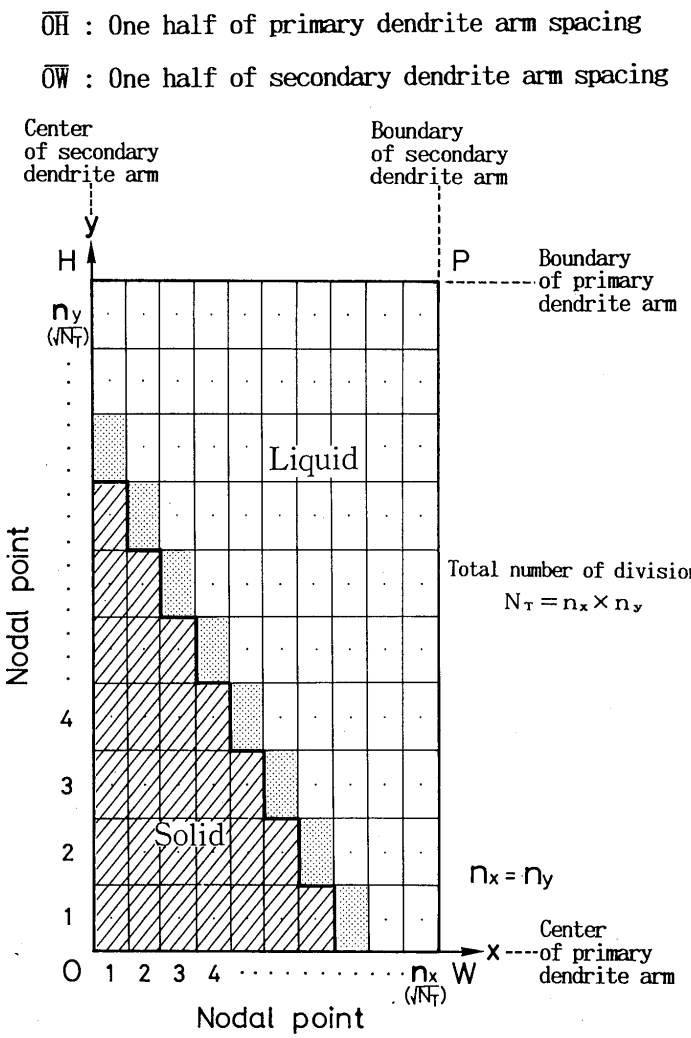

(c) Stepwise growth of solid-liquid interface

Fig. 1 Solidification model of cellular dendrite

interface are neglected.

(4) Melting point depression by solute, namely liquidus gradient is constant irrespective of temperature and concentration.

(5) There is no interaction between solute elements concerning diffusivity, partition coefficient, liquidus gradient.

(6) Coarsening of the secondary dendrite arm spacing near solidification front is neglected.

(7) Volume contraction accompanying solidification is neglected.

(8) Solid-liquid interface advances in a stepwise manner, which is mentioned later.

3.3 Procedures of numerical analysis

This problem is a moving boundary problem, and solved by explicit finite difference method. Therefore, the most important problem is how to advance the solid-liquid interface. In the conventional modellings[6,8,9], the solid-liquid interface generally has a feature of parabolic growth, that is, it advances in proportion to square root of time. In this paper, however, the solid-liquid interface advances so that the liquidus temperature calculated may correspond to the actual temperature: Namely, the dashed region in Fig. 1 (c) corresponds to solidified region, and suppose that solid-liquid interface advances suddenly by dotted zone. This sudden advance the solute concentrations in liquid become higher than those in equilibrium with actual temperature (T_A). In other words, the liquidus temperature (T_C) calculated from the concentrations is lower than T_A. Therefore, the interface must be stopped temporarily until T_C get the same value as T_A by the solute diffusion in solid. Then, the interface advances again suddenly. Whole process is composed of the repeat of sudden advance and temporary pause.

This process is illustrated by the flow chart in **Fig. 2**. Solute concentration in solid at the solid-liquid interface,

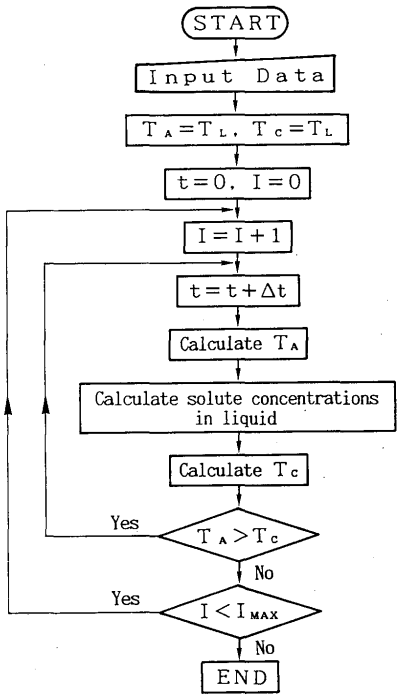

T_L : Initial liquidus temperature
T_A : Actual temperature
T_C : Calculated liquidus temperature
Δt : Time step , I_{MAX} : $2\sqrt{N_T} - 1$

Fig. 2 Flow chart for calculation

C_S (I.J), is always given by Eq. (1) irrespective of sudden advance or temporary pause.

$$C_S(I, J) = k \cdot C_\ell \quad \cdots\cdots (1)$$

where k: equilibrium partition coefficient, C_ℓ: concentration in liquid, I and J are given by a function of the position of solid-liquid interface.

Solute concentration in solid at general nodal point (i, j), C_S (i. j), during temporary pause is given by Eq. (2).

$$C_S(i,j) = C_{SB}(i,j) + D_S \cdot \Delta t/\Delta x^2 \{ C_{SB}(i+1,j) + C_{SB}(i-1,j) - 2C_{SB}(i,j) \} + D_S \cdot \Delta t/\Delta y^2 \{ C_{SB}(i,j+1) + C_{SB}(i,j-1) - 2C_{SB}(i,j) \} \quad \cdots\cdots (2)$$

where C_{SB}: solute concentration just before one time step Δt. D_S: diffusion coefficient in solid phase, Δx, Δy: dimension of a mesh, namely $\Delta x = \overline{OW}/n_x$, $\Delta y = \overline{OH}/n_y$, Δt: time step $< (\Delta x \cdot \Delta y)^2/2D_S(\Delta x^2 + \Delta y^2)$.

According to the assumptions (4) and (5), calculated liquidus temperature T_C is given by Eq. (3) for all elements included.

$$T_C = T_L - \{ m_C([\%C]_\ell - [\%C]) + m_{Si}([\%Si0 - [\%Si]) + m_{Mn}([\%Mn]_\ell - [\%Mn]) + m_P([\%P]_\ell - [\%P]) + \cdots\cdots \} \quad \cdots\cdots (3)$$

where m_X: liquidus gradient by solute X (K/wt.%), $[\%X]_\ell$: concentration of solute X in liquid, [%X] : initial concentration of solute X, T_L: initial liquidus temperture of material.

Actual temperature T_A, is given by Eq. (4)

Table 2 Physical constants of materials used in calculation k: equilibrium partition coefficient, m: liquidus gradient, D_o : vibration factor, Q: activation energy.

Element	in Austenite				in Ferrite			
	k	m (K/wt.%)	D_o (mm^2/sec)	Q (kJ/mol)	k	m (K/wt.%)	D_o (mm^2/sec)	Q (kJ/mol)
C	0.35*	60*	—	—	0.2*	80*	—	—
Si	0.52	7.6	30	251	0.77	12*	800	249
Mn	0.78	4.5*	5.5	249	0.76	5*	76	224
P	0.13	35	1	183	0.23	35	290	230
S	0.035	40	240	223	0.091	40	456	215
Cr	0.88	0.8	6.3	252	0.99	0.96*	6	212
Ni	0.94	0.4	0.9	251	0.77	3**	970	262
Mo	0.81	1.9	3.6	240	0.91	1.9	78.5	226

* : Estimated from binary phase diagram[15]
** : Estimated from Fe-Cr-Ni equilibrium phase diagram[16]
k : Ref.17 for P, Ref.18 for S in δ, Ref.19 for Cr and Ni in γ, Ref.20 for Cr and Ni in δ, Ref.21 for Mo, Ref.22 for the other elements
m : Ref.18 for Cr and Ni in γ, Ref.23 for Mo, Ref.22 for the other elements
D_o and Q : Ref.24 for Cr and Ref.25 for Ni in γ, Ref.26 for Ni in δ, Ref.22 for the other elements

$$T_A = T_L - R_C \cdot t \quad \cdots\cdots (4)$$

where R_C is the cooling rate of weld metal.

3.4 Physical constants and other conditions used for calculation

Concentrations of C, Si, Mn, P, S, Cr, Ni and Mo were numerically analyzed simultaneously in this modelling, and their equilibrium partition coefficient k, liquidus gradient m, vibration factor D_o and activation energy Q to calculate diffusivity in solid are listed in **Table 2** with their references.

The cooling rate used was 250K/sec, which was measured under the same condition of the Trans-Varestraint test[1]. The primary and the secondary dendrite arm spacings used were 20 and 6μm respectively which were measured in quenched weld metals by the linear intercept method.

The division number n_x (= n_y) used was 20 and 16 on the basis of the calculated BTR which will be shown in the next paper[13]. This means N_T is 400 and 256, respectively.

4. Results and Discussion

4.1 Temperature of solid bridge formation

Calculated relations between temperature and fraction solid f_S in SUS310S, SUS430 and SUS329J2L are shown in **Fig. 3**. The broken line means the relation in the case of parabolic growth. The lower limit of BTR means the temperature where solidification is completed. As mentioned in 3.1, the beginning of solid bridge is formed at $f_S = 0.5$.

Typical characteristics can be seen in SUS310S shown in **(a)**. The temperature where the beginning of solid bridge is formed is 1666K in the model, namely only 7K beneath the solidification front. This well corresponds to the observation by liquid-tin quenching in the previous paper[2-4], although the observed temperature seems somewhat higher than the calculated ones. Therefore, the model means that small amount of liquid which is confined by the solid bridges remains for very long period in the BTR. For example, the temperature region where f_S is larger than 0.9 covers about 1650 to 1527K. This tendency also corresponds well to the observation by liquid-tin quenching[2-4]. Therefore, the two dimensional modelling proposed in this paper gives reasonable results. On the contrary, the calculated temperature of solid bridge formation in the case of parabolic growth is too low compared with the observation. Under this condition, the temperature region where f_S is larger than 0.9 covers

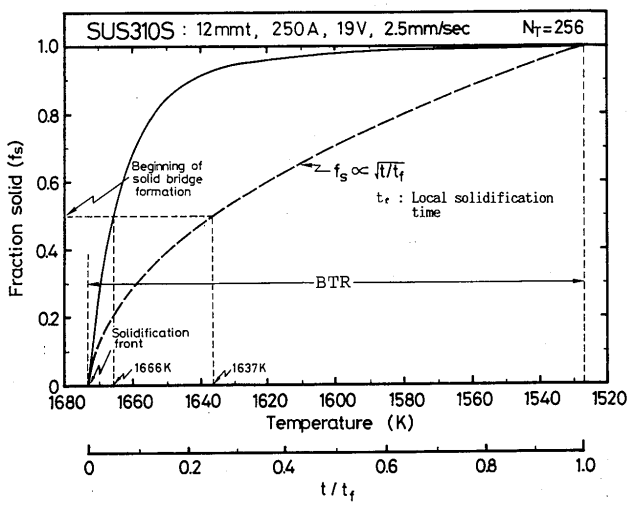

(a) SUS310S

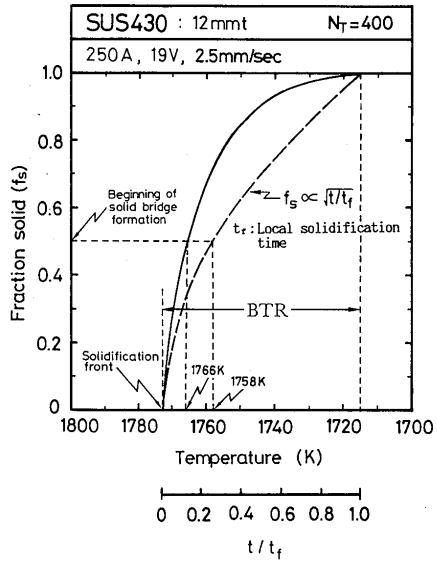

(b) SUS430

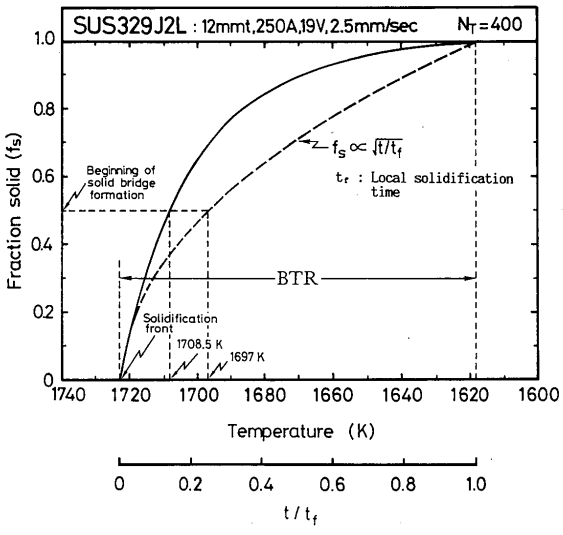

(c) SUS329J2L

Fig. 3 Change in fraction solid during weld solidification

only about 1550 to 1527K. These tendencies do not fit with the observation by liquid-tin quenching[2-4]. By the way, **Fig. 4** shows the tendency of solute enrichment into the residual liquid in SUS310S, and means that P, S and Si are prone to concentrate. These are in good agreement with the experimental results[27,28] which showed an evidence that traces of liquid droplets enriched with mainly P or S and sometimes with Si in a lower temperature region of BTR.

The behaviors in SUS430 and SUS329J2L are shown in Fig. 3 **(b)** and **(c)**, in which nitrogen is taken account of because of the reason mentioned in the next paper[13]. In both cases, fundamental behavior is the same as in (a). The temperature region between the temperature of solid bridge formation and the lower temperature limit of BTR is very small in SUS430, and medium in SUS329J2L. These behaviors well correspond to the observation by liquid-tin quenching[2-4].

4.2 Solute distribution in cellular dendrite

The solid curves in **Fig. 5 (a)** shows isoconcentration curve of Ni just at the completion of solidification in SUS310S. The simbols O, H, P and W in the four corners are the same as in Fig. 1, and the abscissa and the ordinate are normalized by $\overline{OW}$ and $\overline{OH}$, respectively. The numerals in parentheses attached to the broken lines mean Ni concentrations in solid which was located at the solid-liquid interface during solidification. All of the solid curves almost correspond to the broken lines, because of very slow diffusivity of Ni. Therefore, there is very little difference in Ni distribution along $\overline{HP}$ and $\overline{WP}$ as shown in

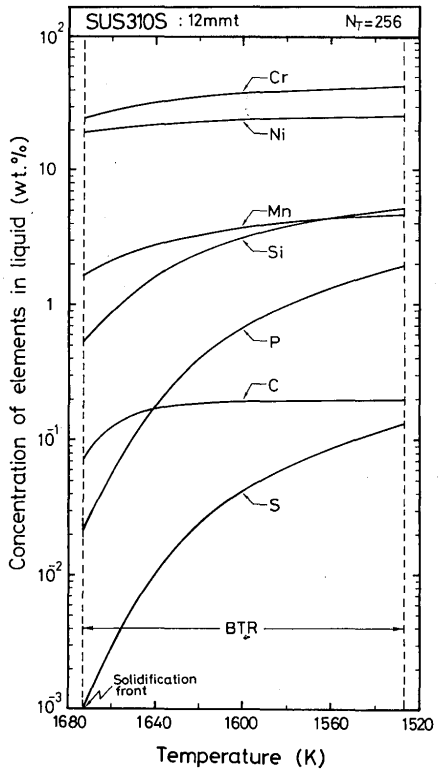

Fig. 4 Change in concentration of elements in residual liquid during weld solidification of SUS310S.

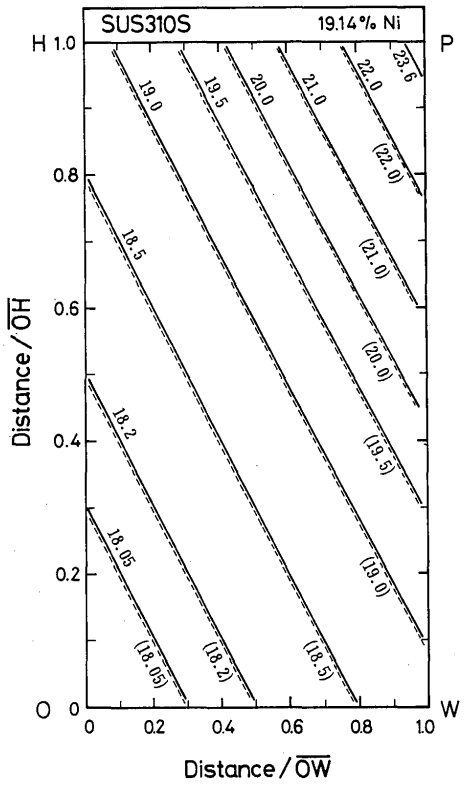

(a) Isoconcentration curve

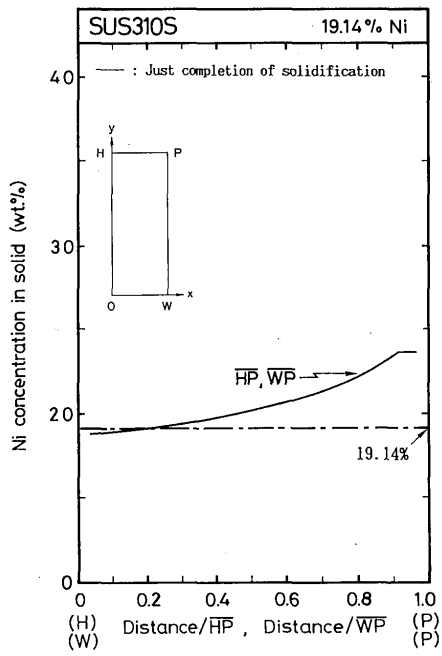

(b) Distribution along cellular dendritic boundary

Fig. 5 Distribution of Ni concentration in cellular dendrite near the lower temperature limit of BTR in SUS310S
$\overline{HP}$: primary dendrite arm boundary.
$\overline{WP}$: secondary dendrite arm boundary

Fig. 5 **(b)**, although Ni along $\overline{WP}$ is somewhat lower than along $\overline{HP}$.

Comparison between the calculated and experimentally analyzed Ni concentration is given in **Fig. 6**. The alphabetical letters used to denote the analyzed locations are defined in the upper right corner.

Solid circles mean the experimentally analyzed concentration, and triangles mean the calculated concentration. Open circles mean calculated average concentration within circle of 1μm radius considering the size of X-ray generating region in EPMA analysis. It should be noticed that the calculated results agree well with the experimental results except a small disagreement at the point P.

Figure 7 (a) and **(b)** show the distribution of Cr just at the completion of solidification in SUS310S. As a whole, the tendency is similar to Ni shown in Fig. 5 except somewhat bigger segregation of Cr. **Figure 8** gives the comparison between the calculated and experimentally analyzed Cr concentrations. All the simbols have the same definitions as in Fig. 6. It is seen that the calculated results generally agree well with the experimental results except the points P and O. The authors considered that these disagreements were mainly caused by the error of equilibrium partition coefficient. For example, **Fig. 9** shows the comparison between the experimental and the calculated results which were obtained by Cr partition coefficient of 0.92, only 5% bigger partition coefficient than Fig. 8. The calculated results agree satisfactorily with the experimental results. Since the diffusivity of Cr in solid may be another reason for the disagreements at the points P and O in Fig. 8, four times faster diffusivity was used in the calculation as a trial at the fixed partition coefficient. Although the disagreements were improved,

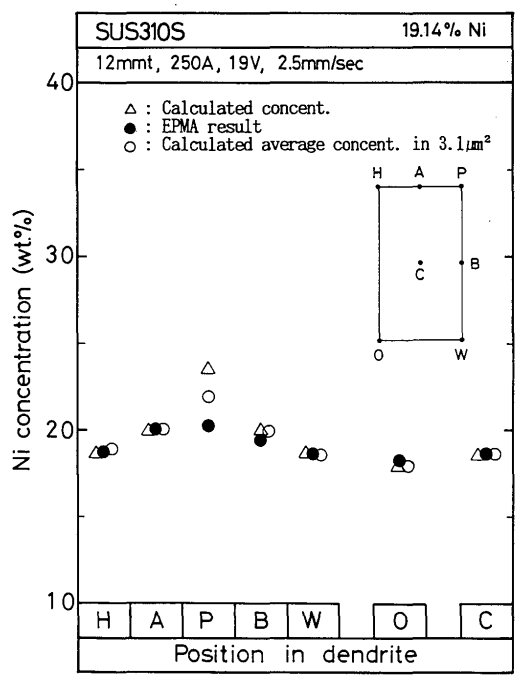

Fig. 6 Comparison between calculated and experimentally analyzed Ni concentrations in cellular dendrite of SUS310S.

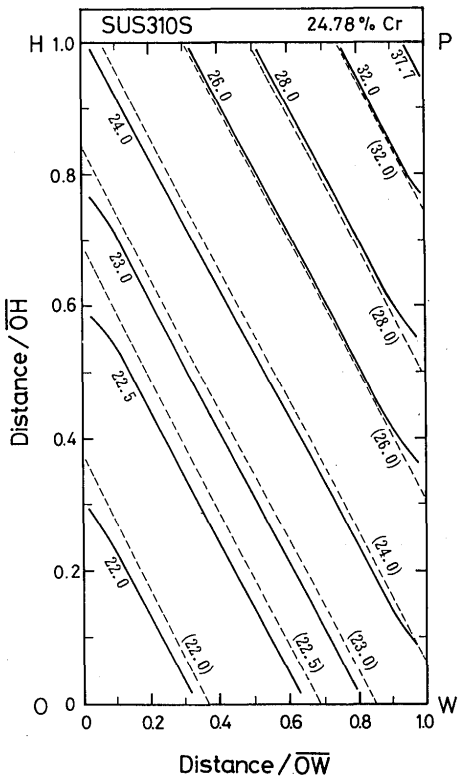

(a) Isoconcentration curve

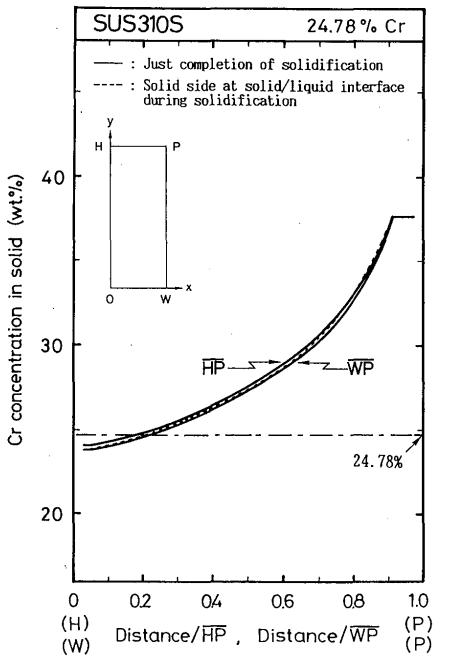

(b) Distribution along cellular dendritic boundary

Fig. 7 Distribution of Cr concentration in cellular dendrite near the lower temperature limit of BTR in SUS310S
$\overline{HP}$: primary dendrite arm boundary,
$\overline{WP}$: secondary dendrite arm boundary

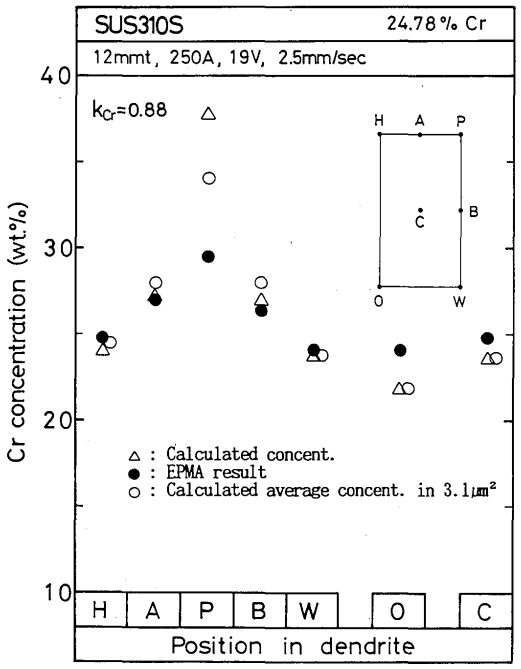

Fig. 8 Comparison between calculated and experimentally analyzed Cr concentrations in cellular dendrite of SUS310S, k_{Cr} of 0.88 was used.

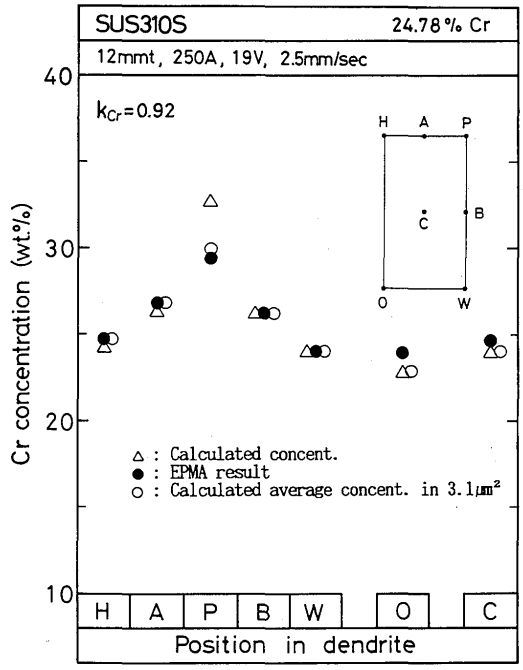

Fig. 9 Comparison between calculated and experimentally analyzed Cr concentrations in cellular dendrite of SUS310S, k_{Cr} of 0.92 was used.

but not so satisfactory as seen in Fig. 9.

Figure 10 (a) shows isoconcentration curve of Ni just at the completion of solidification in SUS329J2L. The definition of solid and broken curves are the same as in the results of SUS310S. In this case, the solid curves fairly deviate from the broken curves because of relatively faster

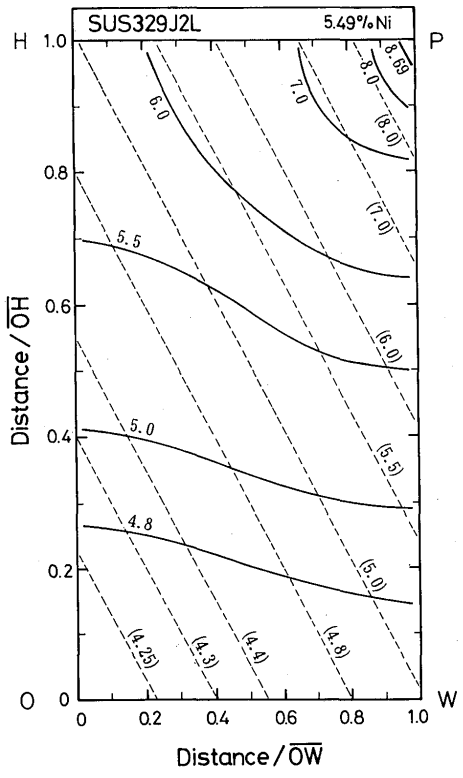

(a) Isoconcentration curve

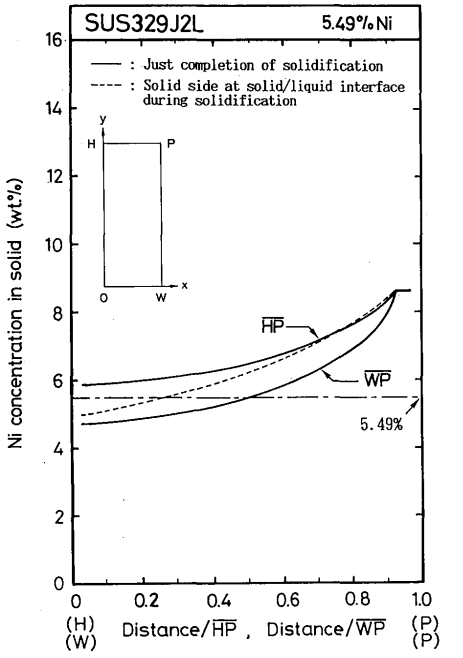

(b) Distribution along cellular dendritic boundary

Fig. 10 Distribution of Ni concentration in cellular dendrite near the lower temperature limit of BTR in SUS329J2L
$\overline{HP}$: primary dendrite arm boundary,
$\overline{WP}$: secondary dendrite arm boundary

diffusivity of Ni in ferrite. Especially near $\overline{OW}$, isoconcentration curve is nearly horizontal. This means that Ni is almost uniform along $\overline{OW}$. Therefore, Ni distribution

along $\overline{WP}$ is definitely lower than that along $\overline{HP}$ as shown in Fig. 10 **(b)**.

Comparison between the calculated and the experimentally analyzed Ni concentrations is given in **Fig. 11**. A good correspondence between the calculated and the analyzed results can be seen. It should be noticed that the concentration at B is definitely lower than A, and that the concentration at W is also definitely lower than H. This tendency was not clearly seen in Fig. 6, and this is because of the faster diffusivity of Ni in ferrite. Similar difference in ferrite and austenite was seen in calculated distributions of S and P, which will be shown next in Fig. 14 (b) and Fig. 15 (b), and it might be explained by the well known fact that solute diffusivity in ferrite is generally faster than in austenite. The reason why the secondary dendrite arm boundary becomes obscure faster than the primary dendrite arm boundary[2-4] in the solidification mode with primary ferrite may be explained by these behaviors.

Figure 12 (a), (b) and **Fig. 13** show the behaviors of Cr in SUS329J2L, and a good correspondence between the calculated and the analyzed results can be seen.

Therefore, it is concluded the two dimensional modelling of cellular dendrite proposed in this paper is generally satisfactory and very useful.

As well known, phosphorus and sulphur segregation are generally very important from the viewpoint of solidification cracking, but it is actually very difficult to analyze their distribution in dendrite because of their low content and low solubility. Then for information, **Fig. 14** and **Fig. 15** show phosphorus distribution in SUS310S and SUS329J2L, respectively. The segregation of phosphorus in SUS310S is severer than SUS329J2L because of smaller partition coefficient and slower diffusivity.

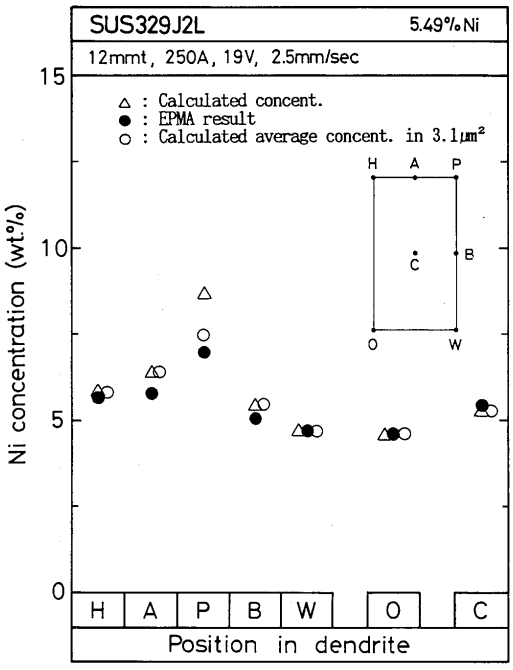

Fig. 11 Comparison between calculated and experimentally analyzed Ni concentrations in cellular dendrite of SUS329J2L.

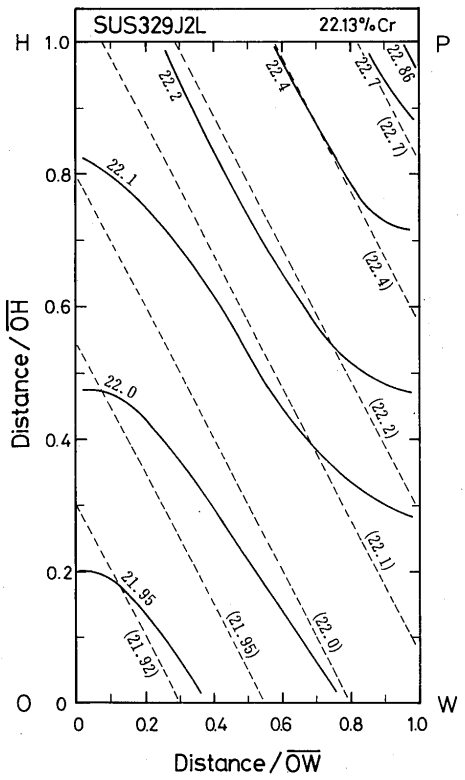

(a) Isoconcentration curve

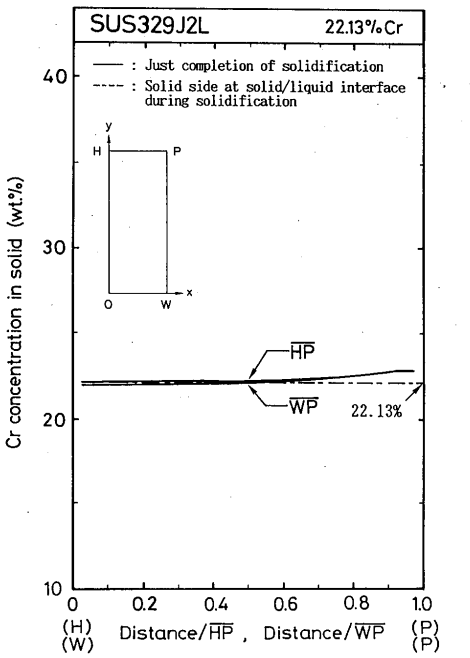

(b) Distribution along cellular dendritic boundary

Fig. 12 Distribution of Cr concentration in cellular dendrite near the lower temperature limit of BTR in SUS329J2L
$\overline{HP}$: primary dendrite arm boundary,
$\overline{WP}$: secondary dendrite arm boundary

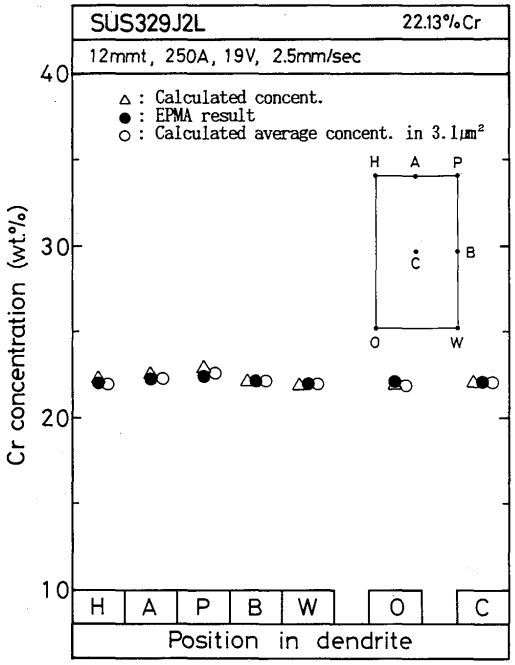

Fig. 13 Comparison between calculated and experimentally analyzed Cr concentrations in cellular dendrite of SUS329J2L.

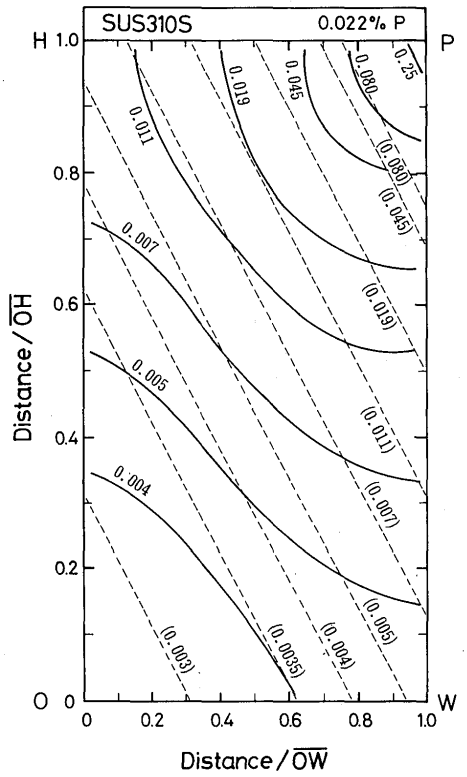

(a) Isoconcentration curve

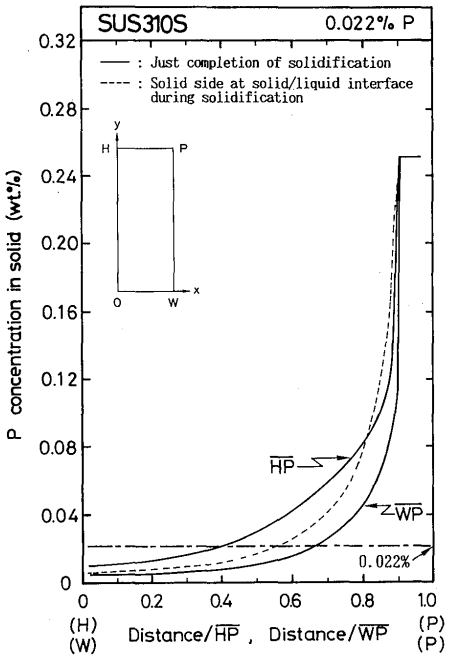

(b) Distribution along cellular dendritic boundary

Fig. 14 Distribution of P concentration in cellular dendrite near the lower temperature limit of BTR in SUS310S
$\overline{HP}$: primary dendrite arm boundary,
$\overline{WP}$: secondary dendrite arm boundary

5. Conclusion

A two dimensional modelling of cellular dendritic growth during weld solidification was made based on the microstructures of stainless steels which were revealed by liquid-tin quenching. In the modelling, the solid bridge is formed when fraction solid is 0.5. Solid-liquid interface advances so that the liquidus temperature of liquid may correspond to the actual temperature. The results calculated for fully austenitic, ferritic and duplex stainless steel were compared with EPMA results.

Main conclusions obtained are as follows:

(1) In this modelling, fraction solid increases very rapidly near liquidus temperature, and thus the temperature where the beginning of solid bridge is formed is very close to the liquidus temperature.

(2) Therefore, the temperature zone where residual liquid is confined by the solid bridges is very long.

(3) These behaviors mentioned in (1) and (2) fit well with the actual solidification microstructures. On the other hand, the behaviors calculated by parabolic growth model where solid-liquid interface advances in proportion to square root of time do not fit with the actual microstructure.

(4) Distribution of Ni and Cr in cellular dendrite calculated by this modelling corresponds well to the analyzed results. Namely, (i) Ni and Cr concentration is the highest at the intersectional site of primary and secondary dendrite arm boundary. (ii) The concentration in primary dendrite arm boundary is higher than that in secondary dendrite arm boundary. (iii) This concentration difference is remarkable in the weld metal solidifying with ferrite phase compared with that with austenite phase.

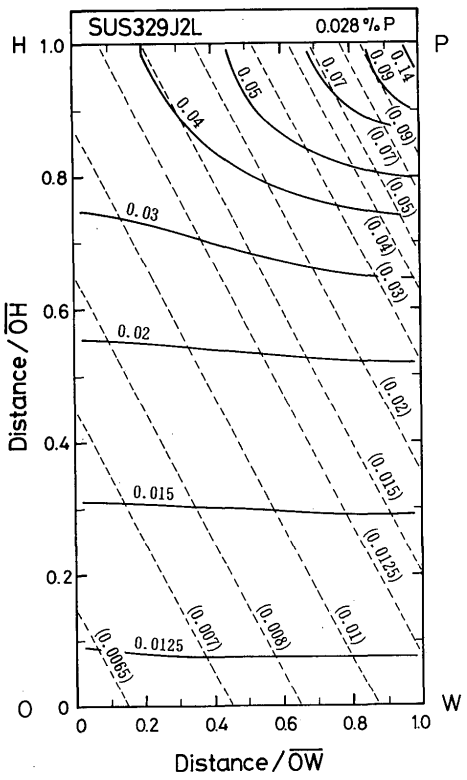

(a) Isoconcentration curve

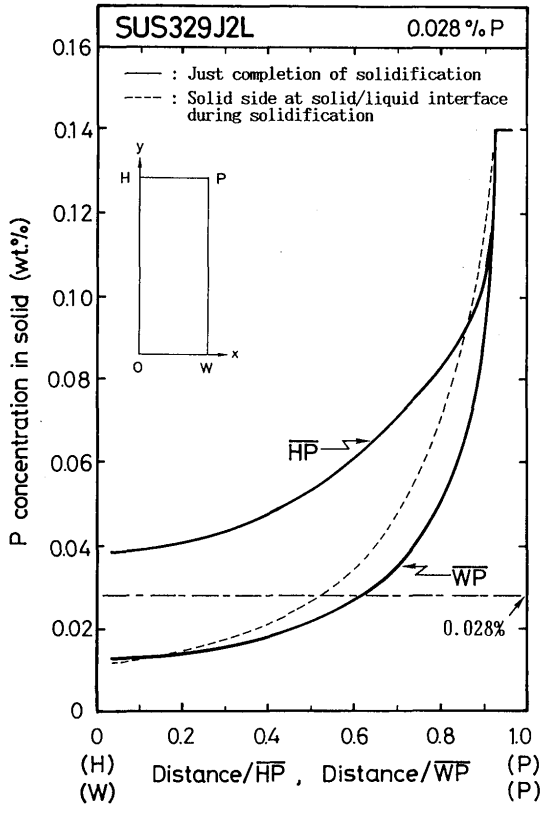

(b) Distribution along cellular dendritic boundary

Fig. 15 Distribution of P concentration in cellular dendrite near the lower temperature limit of BTR in SUS329J2L
$\overline{HP}$: primary dendrite arm boundary,
$\overline{WP}$: secondary dendrite arm boundary

(5) Therefore, the two demensional modelling proposed is very useful to estimate quantitatively the sequence of solidification and the development of solute segregation.

Acknowledgement

The authors would like to thank Mr. T. Hirose, and Mr. M. Yamamoto, formerly students of Kinki Univ., for their cooperation in the experiment, and Sumikin Welding Industries, Ltd. for its supply of materials used.

Reference

1) F. Matsuda, H. Nakagawa, K. Kato and Y. Murata: Trans. of JWRI, **15**-1 (1986), 99–112.
2) F. Matsuda, H. Nakagawa and J.B. LEE: Trans. of JWRI, **16**-2 (1987), 115–121.
3) F. Matsuda, H. Nakagawa and J.B. LEE: Quarterly J. of JWS, 7–2 (1989), 229–234 (in Japanese)
4) F. Matsuda, H. Nakagawa and J.B. LEE: Quarterly J. of JWS, 7–2 (1989), 225–239 (in Japanese)
5) E. Scheil: Z. Metallk., **34** (1942), 70–72.
6) H.D. Brody and M.C. Flemings: Trans. TMS-AIME, **236**–5 (1966), 615–624.
7) T.W. Clyne and W. Kurz: Metal. Trans., **12A**-6 (1981), 965–971.
8) I. Ohnaka: Trans. ISIJ, **26** (1986), 1045–1051.
9) S. Kobayashi: *Tetsu-to-Hagané.* **71** (1985), S199, S1068 (in Japanese)
10) T. Matsumiya, H. Kajioka, S. Mizokuchi, Y. Ueshima and H. Esaka: Trans. ISIJ, **24** (1984), 873–882.
11) D.G. McCartney and J.D. Hunt: Metal. Trans., **15A**-6 (1984), 983–994.
12) J.D. Hunt and D.G. McCartney: Acta metall., **35**-1 (1987), 89–99.
13) F. Matsuda, H. Nakagawa and J.B. LEE: Trans. of JWRI, **18**-1 (1989), 119–126.
14) H. Nakagawa, F. Matsuda and T. Senda: Trans. of JWS, **5**-2 (1974), 84–89.
15) T.B. Massalski: "Binary Alloy Phase Diagrams" ASM (1986).
16) V.G. Rivlin and G.V. Raynor: International metals reviews, **1** (1980), 21–38.
17) Y. Nakamura and H. Esaka: *Tetsu-to-Hagané,* **67**-4 (1981), S140 (in Japanese).
18) K. Nishikawa, K. Ito and K. Sano: *Tetsu-to-Hagané,* **56**-12 (1970), 1467–1476 (in Japanese).
19) T. Okamoto, K. Kishitake and K. Murakami: Trans. ISIJ, **21** (1981), 641–648.
20) U. Siegel, H.J. Spies and H.J. Eckstein: Mater. Technol., **57**-1 (1986), 25–32.
21) Ö. Hammar and U. Svensson: "Solidification and Casting of Metals" The Metals Soc., London (1979), 401–410.
22) *Tekko-no-Gyoko* (Solidification of Steel), Supplement, Solidification Comm. of ISIJ, ISIJ, Tokyo (1977).
23) T. Fujii, D.R. Poirier and M.C. Flemings: Metal. Trans., **10B**-9 (1979), 331–339.
24) P.J. Alberry and C.W. Haworth: Met. Sci., 8 (1974), 407–412.
25) R.A. Perkins: Metal. Trans., **4**-6 (1973), 1665–1669.
26) D.B. Moharil, I. Jin and G.R. Purdy: Metal. Trans., **5**-1 (1974), 59–63.
27) Y. Arata, F. Matsuda and S. Katayama: Trans. of JWRI, **5**-2 (1976), 35–51.
28) F. Matsuda, H. Nakagawa, S. Ogata and S. Katayama: Trans. of JWRI, 7-1 (1978), 59–70.